SUPPLEMENTAL DATA

Motor Behavior Activates Bergmann Glial Networks

Axel Nimmerjahn,[1] Eran A. Mukamel,[1] and Mark J. Schnitzer[1,2]

[1]James H. Clark Center for Biomedical Engineering & Sciences

[2]Howard Hughes Medical Institute

Stanford University, 318 Campus Drive West, Stanford, CA 94305, USA

TABLE OF CONTENTS

SUPPLEMENTAL DISCUSSION

Ca^{2+} Burst Propagation Mechanism

Given that bursts expand outwards from a central initiation point, Ca^{2+} excitation might be initiated by the diffusion of a small molecule trigger, such as ATP. If such a trigger molecule was released from the central spot and its diffusion was the rate-limiting step in burst propagation, then the leading edge of Ca^{2+} excitation should propagate outward so that its displacement from the center is proportional to the square root of the time elapsed since burst initiation. More complicated models in which the trigger molecule is re-released during burst propagation can lead to other time dependencies, including constant propagation speeds. Since bursts only propagated over tens of microns, our data did not allow us to discriminate among these possibilities. Even when we examined the bursts with the highest signal to noise levels, we could only estimate an approximate 3D diffusion constant (~150 $\mu m^2/s$; n = 13 events, 4 mice) or propagation speed (~10 $\mu m/s$; n = 11 events, 4 mice) in the two respective scenarios.

Ca^{2+} Burst Termination Mechanism

Although γDGG did not significantly alter the frequency of bursts, it did lengthen bursts' duration by reducing the rate constant k_2 in our kinetic model of two reaction steps. Thus, although glutamate transmission is not required for burst initiation, blockade of glutamate transmission does affect the termination of bursts. This could be because the normal termination reaction sequence involves either glutamate reception, or signaling by a molecule downstream of glutamate reception, which slows down to become rate-limiting when glutamate mediated pathways are blocked. Alternatively, a substitute termination reaction could replace the normal means of burst termination when glutamate reception is blocked. In vitro, blockade of AMPA glutamate receptors did not eliminate electrically evoked bursts, but did eradicate an initial component of the $[Ca^{2+}]$ increase in Bergmann glia that was small compared to the component sensitive to PPADS (Piet and Jahr, 2007). However, the available data do not permit us to make more precise conclusions about what glutamate's specific role might be.

SUPPLEMENTAL FIGURES

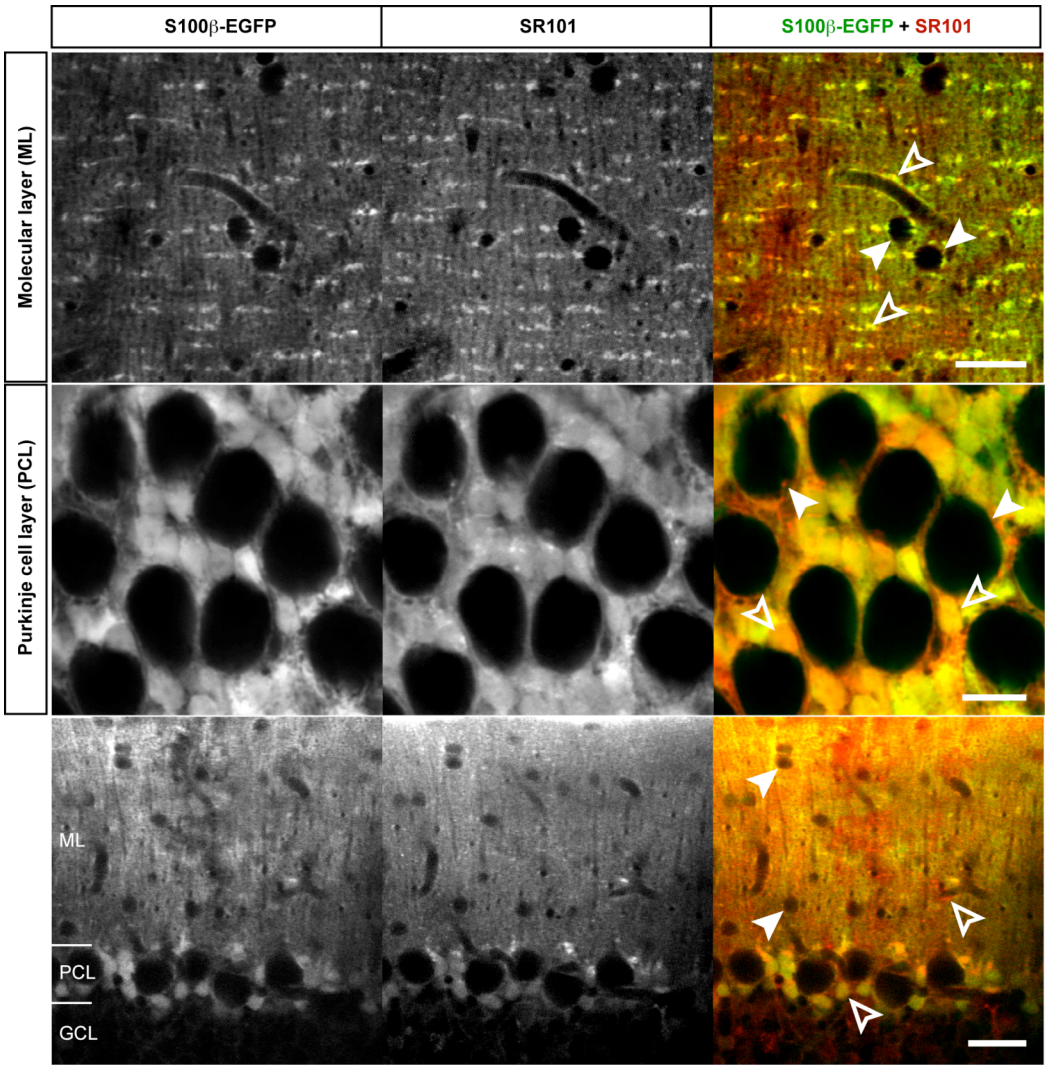

Figure S1. SR101 Co-labeling in S100β-EGFP Mice

Fluorescence images showing EGFP (left column) and SR101 (center column) staining patterns in the molecular (top and bottom rows) and Purkinje cell layers (middle and bottom rows) of an anesthetized, adult S100β-EGFP mouse in which the astrocyte marker SR101 was topically applied to cerebellar cortex. The right column shows the overlays of the green and red fluorescence images, with yellow indicating regions of co-localization. The images in the bottom row were recorded near a bend in the cerebellar folium, which allowed the molecular, Purkinje cell, and granule cell layers to be visualized within a single image. The overlay of images from the molecular layer (top row, right) shows that SR101 stains primary Bergmann glial fibers (open arrowheads) that are arranged in a palisade-like fashion. The fine protrusions emanating from main Bergmann glial fibers are also stained across the molecular layer, but these fine fibers cannot be resolved individually. Molecular layer interneurons (closed arrowheads) are not stained by SR101. Scale bar, 20 μm. The overlay of images from the Purkinje cell layer (middle row, right) shows that SR101 stains Bergmann glia somata (open arrowheads) surrounding Purkinje cell bodies (closed arrowheads). Scale bar, 15 μm. The overlay image in the bottom row shows that SR101 localizes to regions occupied by Bergmann glia somata and processes (open arrowheads). Cell bodies in the molecular layer (closed arrowheads) are not stained by SR101. Velate astrocytes in the granule cell layer (GCL) also appear stained by SR101, but the diminished penetration of both light and the dye compromise imaging at this depth. Scale bar, 30 μm.

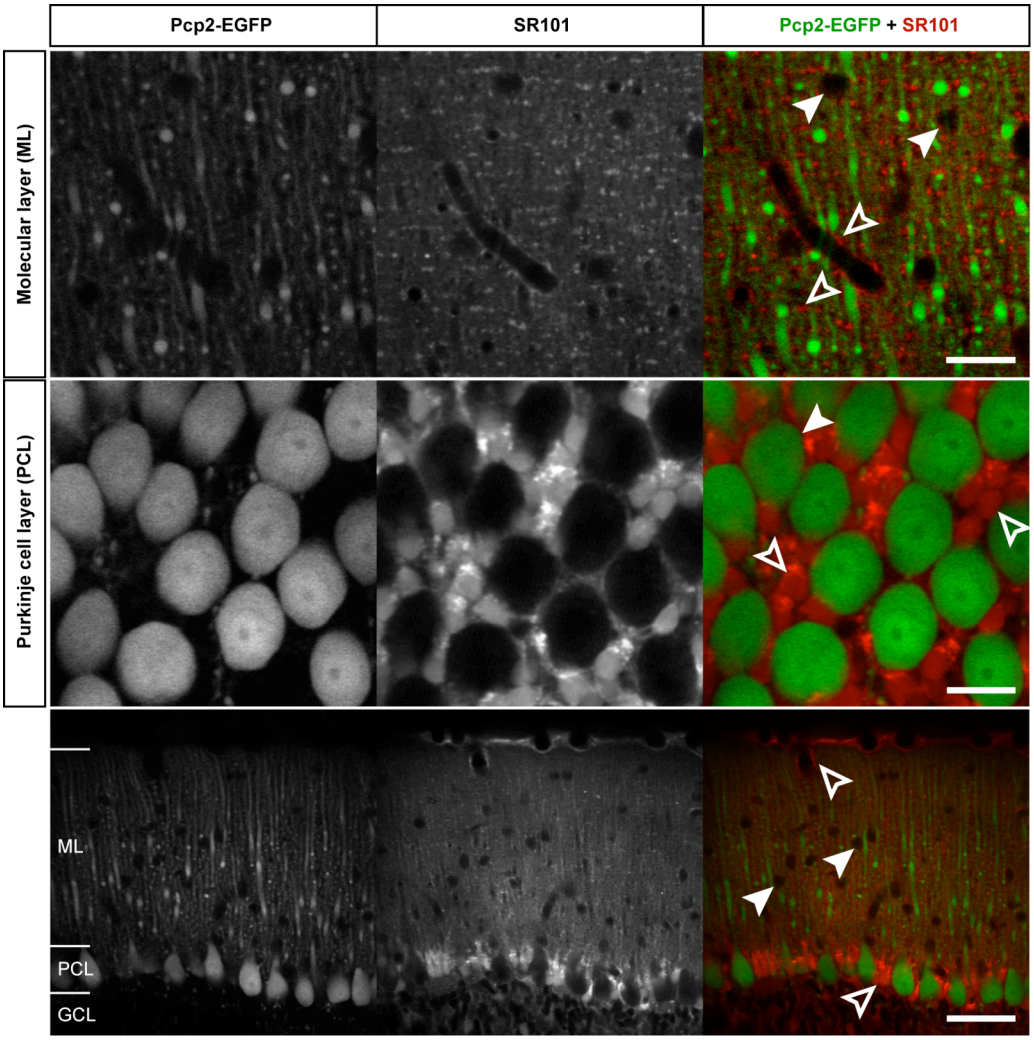

Figure S2. SR101 Co-labeling in Pcp2-EGFP Mice

Fluorescence images showing EGFP (left column) and SR101 (center column) staining patterns in the molecular (top and bottom rows) and Purkinje cell layer (center and bottom rows) of an anesthetized Pcp2-EGFP mouse, in which the astrocyte marker SR101 was topically applied to cerebellar cortex. The right column shows the overlays of the green and red fluorescence images. The images in the bottom row were recorded near a bend in the cerebellar folium, which allowed the molecular, Purkinje cell, and granule cell layers to be visualized within a single image. The overlay of images from the molecular layer (top row, right) shows the distinct and non-overlapping arrangements of EGFP-expressing Purkinje cell dendrites (green) and SR101-stained fibers (red, open arrowheads). Molecular layer interneurons (closed arrowheads) are not labeled by either EGFP or SR101. Scale bar, 20 μm. The overlay of images from the Purkinje cell layer (middle row, right) shows that SR101 stains Bergmann glial somata (open arrowheads) surrounding Purkinje cell bodies (green somata, closed arrowhead), as also shown in Figure S1. Scale bar, 20 μm. The overlay in the bottom row permits multiple characteristic morphological features of SR101-labeled Bergmann glia to be visualized within a single image; SR101 brightly labels Bergmann glial cell bodies in the Purkinje cell layer, as well as glial processes extending into the molecular layer where some have end feet contacts upon blood vessels (open arrowheads). Cell bodies located in the molecular layer (closed arrowheads) are not stained by either EGFP or SR101. Velate astrocytes in the granule cell layer (GCL) also appear stained by SR101, but the diminished penetration of both light and the dye compromise imaging at this depth. Scale bar, 50 μm.

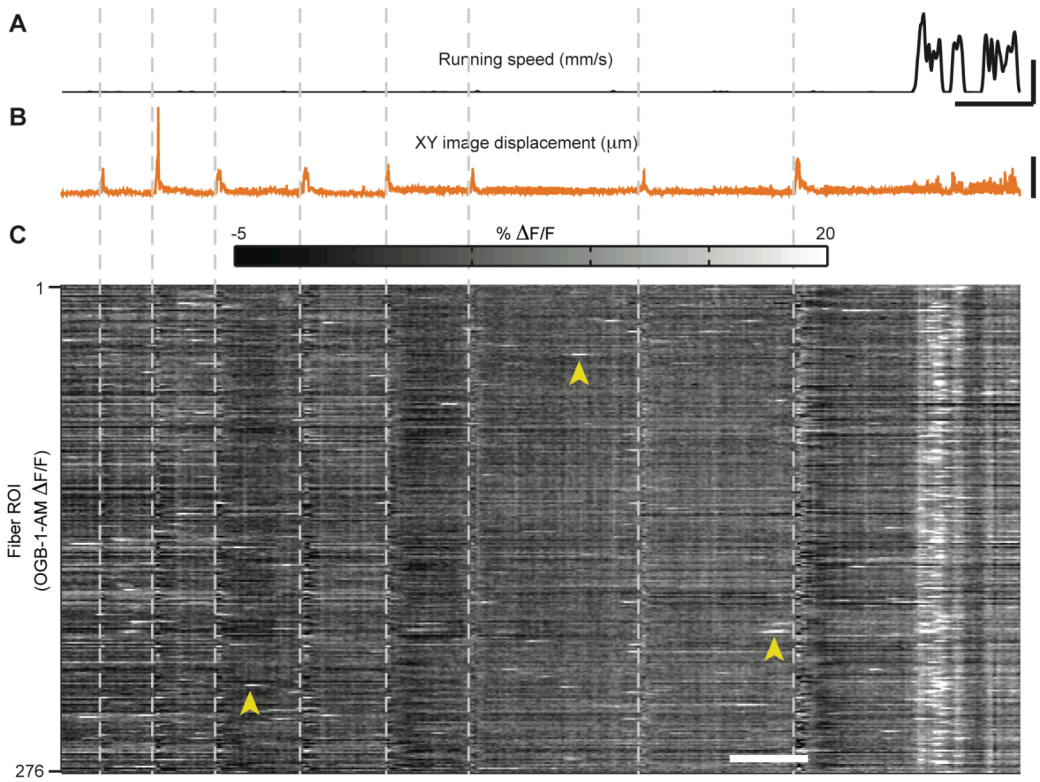

Figure S3. Application of Pressure upon the Cranial Window Does Not Evoke Ca^{2+} Flares

(A) Encoder trace of rotational speed of the exercise ball, showing mouse locomotor activity during a 10.2 min period. Scale bars, 50 s and 50 mm/s.

(B) Absolute value of lateral (*x*-*y*) image displacements during the same time interval as in (A). Dashed lines indicate the times at which pressure of varying amplitude and duration was applied to the cranial window. Note that the resulting image displacements were greater than those that accompanied running. Scale bar, 5 μm.

(C) OGB-1-AM $\Delta F(t)/F$ traces from 276 Bergmann glial fiber regions of interest (ROI), during the same time interval as in (A). The traces are arranged according to the *x*-coordinates of the ROIs within the field of view. The onset of locomotor activity, but not pressure applications, evokes concerted Ca^{2+} activation of Bergmann glial fibers. Note that sparkles within individual ROIs arose independently of pressure applications; a few example sparkles are marked with yellow arrowheads. Scale bar, 50 s.

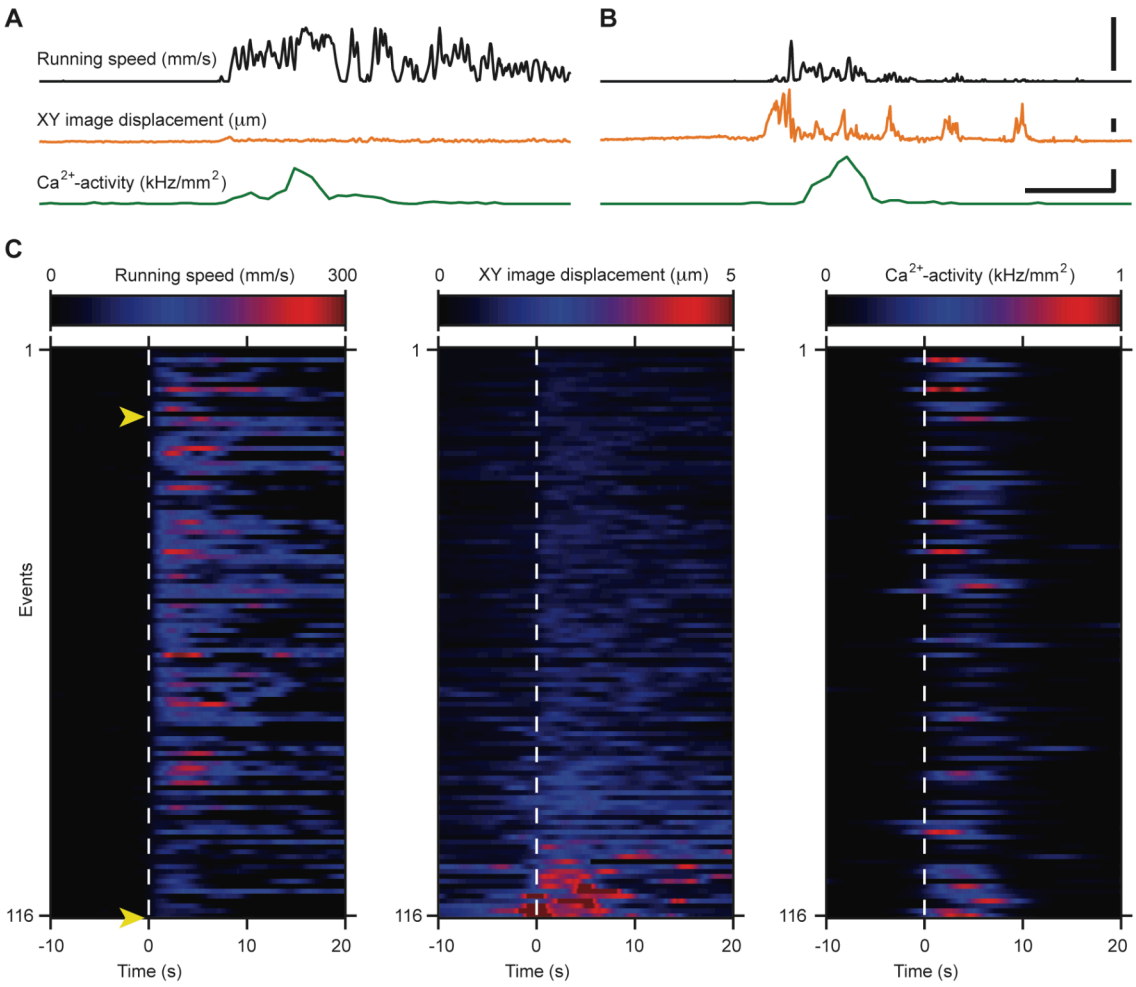

Figure S4. Ca^{2+} Flares Occur Independently of Brain Displacements

(A) An example set of traces illustrating the occurrence of a Ca^{2+} flare in the absence of measurable brain displacement. The traces show simultaneous records of Ca^{2+} activity summed over 370 glial fiber ROIs (green), the absolute value of lateral (XY) image displacements (orange), and the mouse's locomotor speed (black). Upper, center, and lower scale bars are the same as in (B).

(B) An example set of traces from a different mouse than in A, illustrating the occurrence of a Ca^{2+} flare in the presence of measurable brain displacement. The traces show simultaneous records of Ca^{2+} activity summed over 233 glial fiber ROIs (green), the absolute value of lateral (XY) image displacements (orange), and the mouse's locomotor speed (black). Note that some brain displacements occurred both prior to and after the running episode. However, the onset of the Ca^{2+} flare occurs within the normal range of time delays following locomotor initiation and shows no obvious temporal relationship to the brain displacements. Upper scale bar, 300 mm/s. Center scale bar, 5 μm. Lower scale bars, 5 s and 1 kHz/mm^2.

(C) Population data showing simultaneous traces of running speed (left), absolute values of lateral (XY) image displacements (center), and Ca^{2+} activity in Bergmann glial fibers (right). The data depict 116 traces of locomotor events from 15 different mice. Dashed lines indicate movement onsets. The traces are arranged from smallest to greatest lateral (XY) image displacements. The yellow arrowheads indicate the two trials shown in (A) and (B).

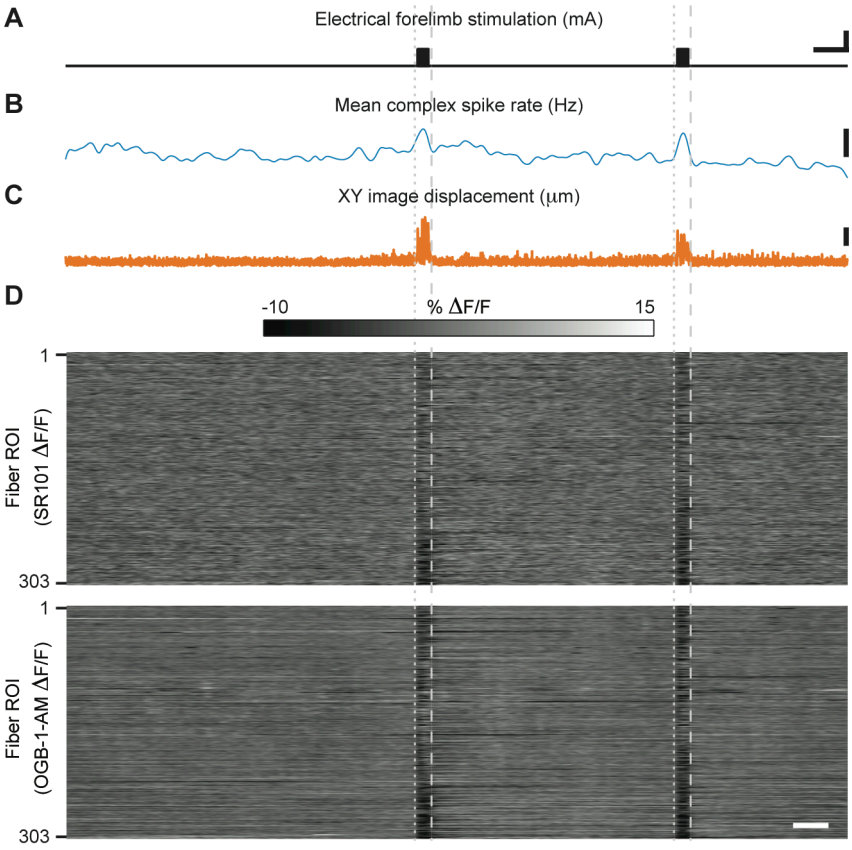

Figure S5. Electrical Limb Stimulation Does Not Evoke Ca^{2+} Flares

(A) Trace showing two periods of electrical forelimb stimulation in an anesthetized mouse during a 3.7 min period. The protocol for electrical stimulation consisted of a train of 60 square pulses, each of 20 ms duration and 10 mA, delivered at 20 Hz. Dotted and dashed lines indicate the onsets and offsets, respectively, of the stimulation protocol. Scale bars, 10 s and 10 mA.

(B) Mean Ca^{2+} spike rate averaged over 9 Purkinje neurons, measured by two-photon Ca^{2+} imaging in the vermis ipsilateral to the forepaw receiving stimulation. Each delivery of electric stimulation led to a visible increase in climbing fiber-evoked Purkinje cell Ca^{2+} spiking. Scale bar, 0.5 Hz.

(C) Absolute value of lateral (XY) brain image displacements during the same time interval as in (A). Images were co-registered to remove lateral displacements prior to analysis of Ca^{2+} activity. Scale bar, 1 μm.

(D) Top, SR101 $\Delta F(t)/F$ traces from 303 glial fiber regions of interest (ROI). Bottom, the same ROIs in OGB-1-AM images that were also used to extract the net complex spike rate shown in (B). Despite the visible neuronal responses, ipsilateral electrical forelimb stimulation did not evoke glial Ca^{2+} flares. Note that under anesthesia sparkles are largely absent (Table S1). Scale bar, 10 s. Glial fibers ROIs were sorted by *x* coordinate.

SUPPLEMENTAL TABLES

Table S1. Properties of Ca^{2+} Sparkles

	Mean ± s.d.	Range	*n*	Animals	*p* value	Statistical test
Amplitude (% $\Delta F(t)/F$):						
(a) awake resting	13.2 ± 4.1	10.1 – 134.3	4285	15	-	-
(b) under TTX	12.1 ± 2.8	10.1 – 34.6	277	5	< 0.01	Wilcoxon rank sum
(c) under γDGG	11.9 ± 2.9	10.1 – 49.4	614	4	< 0.01	
(d) under PPADS	12.2 ± 2.5	10.1 – 28.9	974	3	< 0.01	
(e) under isoflurane	11.9 ± 1.8	10.1 – 16.4	14	4	0.25	
Duration (s):						
(a) awake resting	3.3 ± 3.9	0.5 – 35.4	4285	15	-	-
(b) under TTX	2.3 ± 2.6	0.5 – 24.6	277	5	$< 10^{-3}$	Wilcoxon rank sum
(c) under γDGG	3.8 ± 5.5	0.5 – 36.9	614	4	0.32	
(d) under PPADS	2.8 ± 3.2	0.5 – 28.0	974	3	< 0.01	
(e) under isoflurane	2.4 ± 2.1	0.5 – 5.9	14	4	0.10	
Frequency (Hz/mm^2):						
(a) awake resting	4.5 ± 2.6	1.1 – 11.0	4285	15	-	-
(b) under TTX	1.5 ± 0.5	1.0 – 2.2	277	5	$< 10^{-6}$	Likelihood ratio test
(c) under γDGG	3.6 ± 2.3	0.5 – 5.7	614	4	< 0.002	
(d) under PPADS	5.7 ± 2.5	3.3 – 8.4	974	3	> 0.2	
(e) under isoflurane	0.2 ± 0.1	0.0 – 0.3	14	4	$< 10^{-5}$	

Table S2a. Temporal Properties of Ca^{2+} Bursts

	Mean ± s.d.	Range	*n*	Animals	*p* value	Statistical test
Amplitude (% $\Delta F(t)/F$):						
(a) awake resting	12.9 ± 4.8	2.8 – 24.8	96	11	-	-
(b) under TTX	13.8 ± 3.9	5.3 – 17.0	9	5	0.41	Wilcoxon rank sum
(c) under γDGG	8.9 ± 3.1	3.0 – 12.3	7	2	0.025	
(d) under PPADS	7.5 ± 3.6	3.0 – 16.6	18	2	$< 10^{-4}$	
(e) under isoflurane	10.8 ± 6.3	3.9 – 20.8	8	5	0.25	
$1/k_1$ (s)[1]:						
(a) awake resting	1.5 ± 0.7	0.0 – 4.1	96	11	-	-
(b) under TTX	1.5 ± 0.6	0.5 – 2.7	9	5	0.77	Wilcoxon rank sum
(c) under γDGG	2.2 ± 1.2	0.7 – 3.6	7	2	<0.1	
(d) under PPADS	1.4 ± 0.4	0.6 – 2.1	18	2	0.78	
(e) under isoflurane	1.4 ± 0.4	0.7 – 2.0	8	5	0.79	
$1/k_2$ (s)[1]:						
(a) awake resting	1.8 ± 1.2	0.7 – 10.8	96	11	-	-
(b) under TTX	1.6 ± 0.5	1.0 – 2.7	9	5	0.88	Wilcoxon rank sum
(c) under γDGG	9.6 ± 10	3.3 – 30	7	2	< 0.001	
(d) under PPADS	2.7 ± 2.2	1.2 – 9.2	18	2	0.046	
(e) under isoflurane	2.2 ± 1.8	1.1 – 6.5	8	5	0.57	
Frequency (mHz/mm^2):						
(a) awake resting	168 ± 187	36.7 - 566	161	8	-	-
(b) under TTX	41 ± 48	0.0 - 149	38	8	> 0.01 in 7 animals	Likelihood ratio test
(c) under γDGG	28 ± 23	0.0 – 52.9	9	4	> 0.1 in 2 animals	
(d) under PPADS	1.5 ± 3.0	0.0 – 6.1	1	4	< 0.01	
(e) under isoflurane	28 ± 50	0.0 – 214	23	18	> 0.01	

[1] k_1 and k_2 are the rate constants for the burst time course in the two stage model discussed in the text.

Table S2b. Spatial Properties of Ca^{2+} Bursts

	Mean ± s.d.	Range	*n*	Animals
Medio-lateral extent (μm)	55 ± 37	6.9 – 177	63	9
Rostro-caudal extent (μm)	44 ± 33	4.6 – 213	63	9
Axial extent (μm)	56 ± 23	32 - 108	10	5
Volume (μm^3)	86,000 ± 61,000	7,631 - 175,309	10	5

Table S3a. Properties of Ca^{2+} Flares

	Mean ± s.d.	Range	*n*	Animals
Time from flare onset to peak (s)	4.2 ± 1.4	1.2 – 8.2	93	15
Mean duration (s)	9.7 ± 2.8	3.2 – 18.6	93	15
Occurrence probability[1] (%) as a function of inter-movement pause:				
(a) 1.0 – 2.0 s	14.3 ± 15.8	-	14	15
(b) 2.0 – 4.0 s	7.41 ± 8.95		27	15
(c) 4.0 – 8.0 s	12.5 ± 14.2		16	15
(d) 8.0 – 16.0 s	25.0 ± 11.9		24	15
(e) 16.0 – 32.0 s	57.1 ± 16.7		14	15
(f) 32.0 – 64.0 s	85.7 ± 15.8		14	15
(g) > 64.0 s	96.7 ± 4.16		61	15
Flares without measurable ball rotation (%)	6.9 ± 5.9	-	87	15

[1]Probability of observing a flare following an encoder triggered movement

Table S3b. Effect of Various Treatments on Ca^{2+} Flare Occurrence

	Occurrence	*n*	Animals
Control (*awake animal*)	At movement onset (*refractory dynamics*)	187 running bouts	15
Topical TTX application (*awake animal*)	Eliminated	44 running bouts	5
Topical γDGG application (*awake animal*)	Eliminated	45 running bouts	4
Topical PPADS application (*awake animal*)	Not affected	20 running bouts	3
Isoflurane anesthesia	Never	14 recordings	4
Pressure application on cranial window (*anesthetized/awake animal*)	Never	30 stimulations	3
Electrical limb stimulation (*anesthetized animal*)	Never	13 stimulations	3

Table S4a. Median Properties of Locomotion-Triggered Blood Perfusion Increases

	Median ± s.d.	Range	*n*	Animals	*p* value	Statistical test
Time from onset to peak[1] (s)						
(a) awake resting	3.2 ± 28	0.32 – 177	134	11	-	-
(b) under TTX	1.6 ± 3.3	0.25 – 18	35	3	$< 10^{-6}$	Wilcoxon rank sum
(c) under γDGG	1.3 ± 1.0	0.079 – 3.9	45	4	$< 10^{-10}$	
(d) under PPADS	5.5 ± 16	0.66 - 59	47	3	0.011	
Duration[1] (s)						
(a) awake resting	13 ± 36	1.2 - 226	134	11	-	-
(b) under TTX	6.1 ± 6.7	1.4 - 27	35	3	$< 10^{-4}$	Wilcoxon rank sum
(c) under γDGG	7.2 ± 6.2	1.1 - 27	45	4	$< 10^{-5}$	
(d) under PPADS	16 ± 22	1.8 - 87	47	3	0.18	
Amplitude (% of non-movement baseline):						
(a) awake resting	31 ± 11	16 – 68	134	11	-	-
(b) under TTX	21 ± 4.9	15 – 31	35	3	$< 10^{-9}$	Wilcoxon rank sum
(c) under γDGG	23 ± 8.5	15 – 49	45	4	$< 10^{-5}$	
(d) under PPADS	42 ± 12	19 – 60	47	3	0.005	

[1]Values calculated based on all (i.e., brief and extended) movements that are separated by >10 s from the previous movement and show a blood flow increase of >15% over baseline levels within 10 s of movement onset.

Table S4b. Mean Properties of Locomotion-Triggered Blood Perfusion Increases

	Mean ± s.d.	Range	*n*	Animals	*p* value	Statistical test
Time from onset to peak[1] (s)						
(a) awake resting	13 ± 28	0.32 – 177	134	11	-	-
(b) under TTX	2.6 ± 3.3	0.25 – 18	35	3	$< 10^{-6}$	Wilcoxon rank sum
(c) under γDGG	1.5 ± 1.0	0.079 – 3.9	45	4	$< 10^{-10}$	
(d) under PPADS	12 ± 16	0.66 - 59	47	3	0.011	
Duration[1] (s)						
(a) awake resting	24 ± 36	1.2 - 226	134	11	-	-
(b) under TTX	8.4 ± 6.7	1.4 - 27	35	3	$< 10^{-4}$	Wilcoxon rank sum
(c) under γDGG	8.4 ± 6.2	1.1 - 27	45	4	$< 10^{-5}$	
(d) under PPADS	24 ± 22	1.8 - 87	47	3	0.18	
Amplitude (% of non-movement baseline):						
(a) awake resting	34 ± 11	16 – 68	134	11	-	-
(b) under TTX	22 ± 4.9	15 – 31	35	3	$< 10^{-9}$	Wilcoxon rank sum
(c) under γDGG	25 ± 8.5	15 – 49	45	4	$< 10^{-5}$	
(d) under PPADS	39 ± 12	19 – 60	47	3	0.005	

[1]Values calculated based on all (i.e., brief and extended) movements that are separated by >10 s from the previous movement and show a blood flow increase of >15% over baseline levels within 10 s of movement onset.

SUPPLEMENTAL EXPERIMENTAL PROCEDURES

Animals and Surgery

Surgery was done under isoflurane (1.5–2.5%, mixed with 1-2 L/min O_2). Body temperature was monitored with a thermistor underneath the torso and maintained at 36-37°C using a heating blanket. We assessed depth of anesthesia by monitoring pinch withdrawal, eyelid and corneal reflexes, breathing rate, and vibrissae movements.

To note the coordinates studied, we re-anesthetized mice at the end of each experiment and marked recording sites with a water-repellent pen. We removed the brain and made digital images of the marked sites at several magnifications. We overlaid recording sites from different experiments to yield the outline of studied areas (Figure 1B).

Indicator Labeling

Targeted bulk-loading of cerebellar tissue with the Ca^{2+}-indicator Oregon Green 488 BAPTA-1 acetoxymethyl (OGB-1-AM; Molecular Probes) was done as described (Stosiek et al., 2003). To obtain a homogenous, widespread stain of the Purkinje cell and molecular layers we used several pressure ejections (3-3.5 psi; 1-2 min duration; Picospritzer III, General Valve, Fairfield, NJ). Typically five injections were performed in a grid pattern with ~150-250 μm spacing.

31 of the 33 mice used for detailed data analysis received both OGB-1-AM and SR101 labeling, and 2 mice received only OGB-1-AM, but since the results of the Ca^{2+}-imaging data analysis were similar we pooled the data.

Imaging

We used MP-Scope software for laser-scanning microscopy (Nguyen et al., 2006), which uses a 5 MS/s data acquisition card (PCI-6110, National Instruments). For simultaneous excitation of OGB-1-AM and SR101 we ordinarily used 800-820 nm. To obtain the images of Figure 2, and Figures S1 and S2 we used 890 nm.

Behavioral Analysis

Rotations of the exercise ball were monitored using an optical encoder (US Digital, E7PD-720-118). In addition, mouse behavior was recorded in Mini-DV format using a digital Camcorder (Sony DCR-VX2000). Comparison of encoder and video data revealed that the encoder successfully detected not only running and walking but also subtle movements that on the videos were sometimes only barely perceptible by eye. Hence, the encoder provided a sensitive, quantitative, and repeatable readout of running onset/offset, speed and direction.

Pharmacology

TTX (25-125 μM), γDGG (50 mM) and PPADS (1-2 mM) were dissolved in ACSF and applied in aqueous solution onto the optical window in the cranium. To facilitate drug entry into tissue the agarose and cover slip were cut on two sides to be flush with the craniotomy, allowing direct contact between reservoirs of solution and the agarose. Drug action was verified by observing changes in ECoG and that Purkinje cells stained by OGB-1-AM showed a complete silencing of climbing fiber driven Ca^{2+}-spiking activity under TTX and γDGG. Also, TTX sometimes led to changes in mouse gait.

Transgenic Animals

To confirm that the astrocyte marker SR101 (Nimmerjahn et al., 2004) labels Bergmann glia in the cerebellum, we performed dual-color imaging studies of mice expressing EGFP under the control of the human S100β promoter (Zuo et al., 2004) (Kosmos line; age, 6 months) (Figure 2, Figure S1). To confirm that SR101 does not stain cerebellar Purkinje cells, we performed dual-color imaging studies of mice expressing EGFP under the control of the Purkinje cell protein 2 (Pcp2) promoter (Tomomura et al., 2001) (age, 3 months) (Figure S2). Both mouse lines show bright labeling in the cerebellar molecular layer due to ubiquitous expression of EGFP in Bergmann glia processes (S100β-EGFP mice) or Purkinje cell dendrites (Pcp2-EGFP mice), allowing verification that SR101 does not stain molecular layer cell bodies.

General Methods of Image Analysis

We first corrected any lateral motion artifacts in the imaging data using an image registration algorithm (Thevenaz et al., 1998). We corrected for photobleaching and in dual SR101 and OGB-1-AM imaging experiments for overlap in the emission spectra of the two dyes. Regions of interest (ROIs) containing glial fiber palisades were identified in SR101 images by applying a spatial high-pass filter and then finding contiguous regions above a threshold intensity value. To obtain functional Ca^{2+} signals from Bergmann glial fibers, we examined within the OGB-1-AM images the ROI areas that had been identified in the SR101

images to be Bergmann glial palisade ROIs, and from each of these ROIs we extracted traces of normalized fluorescence, $\Delta F(t)/F$ (Figures 3 and 5).

Ca^{2+} sparkles were identified as all instances in which $\Delta F(t)/F$ traces from within an individual glial fiber ROI crossed a threshold value (10%). Ca^{2+} bursts occurred within but were not confined to glial palisades; bursts were readily identified by visual screening of temporally low-pass filtered versions of the movie data.

Ca^{2+} flares were identified as instances in which the instantaneous rate of Ca^{2+} sparkles detected across all of the palisade fiber ROIs within the entire field of view crossed a threshold value (Figures 5 and 6). We used records of the exercise ball's rotational speed to perform reverse correlation analyses, in which we computed the mean rates of sparkling immediately before and after specified patterns of mouse locomotion. See below for more details.

Correction of Movement Artifacts

To correct lateral displacements of the entire field of view, we used the ImageJ plugin *TurboReg* (Thevenaz et al., 1998) to register each movie frame with respect to a reference frame, generally the first frame of the movie, by minimizing the mean square difference between the pixel intensities. Movies were then cropped to the largest region that remained within the field of view throughout the recording duration. To estimate the severity of image displacements during periods of locomotion, we calculated the standard deviation of the displacements used for image registration. Axial displacements were estimated using movies recorded within a coronal optical plane.

Corrections for Overlap in the Emission Spectra of OGB-1-AM and SR101

Due to overlapping emission spectra, we observed modest bleed through of functional OGB-1-AM signals into the red spectral detection channel used to capture fluorescence signals from the non-functional, astrocyte marker SR101. To calibrate this overlap, we used large-amplitude bursts occurring during periods when the mouse was standing still to measure the fixed ratio of OGB-1-AM signals captured on the red and green detection channels. We calculated the relative changes in OGB-1-AM fluorescence detected in each color channel by normalizing each detector's signal by its mean over a brief epoch (<10 s) prior to each burst. We then determined the slope of the line that best fit the co-variation of the two normalized signals, which varied together in a highly linear manner (r = 0.9 ± 0.08). By using data from two or more bursts we were able to fit the slope of the linear dependence between the two channels with <5% uncertainty. For example, the recording used for Figures 5B-D exhibited a bleed through ratio of 0.23 ± 0.008 (95% confidence interval). We multiplied OGB-1-AM signals by this ratio and subtracted the result from the red fluorescence signals to obtain the spectrally unmixed SR101 signals, as shown in Figure 5B.

Corrections for Fluorescence Bleaching

We observed modest (<5%) declines in the mean fluorescence over the entire field of view during each recording lasting <10 min. We compensated for this decline by fitting the traces of normalized fluorescence with an exponentially decaying function. We then divided the fluorescence in each movie frame by the instantaneous value of the fitted decay function. For example, the decay time constants for Figures 5B-D were 53,000 s (OGB-1-AM) and 14,000 s (SR101), which accounted for declines in average fluorescence over the recording of 1.1% and 4.4%, respectively.

Computation of Normalized Changes in Fluorescence, $\Delta F(t)/F$

We normalized traces of fluorescence intensity at each movie pixel by dividing by the mean fluorescence, *F,* over a reference period, generally the entire duration of the recording at that field of view. Data traces were smoothed by convolution with a Gaussian filter of unity gain and either 0.5 s (Figure 3B and 3D) or 0.7 s (Figures 5 and 6) standard deviation. The resulting traces were downsampled to ~2 Hz.

Identification of Glial Palisades

We first averaged the fluorescence intensity in the red detection channel (31 mice), or in the green channel for single-color experiments (2 mice), over all recorded time frames. Glial palisades generally appeared with different intensities relative to background in the two detection channels, and we used the ratio of fluorescence in each channel to emphasize glial-specific peaks in fluorescence. We then sharpened the resulting image by convolving with the 3×3 digital high-pass filter kernel

$$K = \begin{bmatrix} -1 & -1 & -1 \\ -1 & k & -1 \\ -1 & -1 & -1 \end{bmatrix},$$

where *k* was either 8 or 12. We identified regions of interest (ROIs) corresponding to Bergmann glial processes by applying a threshold to the sharpened image and isolating contiguous regions within the resulting binary mask that were no more than ~20 μm^2 in area. In dual-color experiments, we observed that large (>40 μm^2 area), brightly labeled structures in the OGB-1-AM channel generally corresponded to interneuron cell bodies not labeled by the astrocyte marker SR101. We therefore excluded these large ROIs from further analysis in the two mice studied by single-color experiments, for which only OGB-1-AM signals were available.

Detection of Fluorescence Increases within Individual Glial ROIs.

We observed Ca^{2+}-transient related increases in fluorescence within individual glial ROIs during sparkles, bursts, and flares. For each ROI, these transients were identified by finding peaks in the smoothed normalized fluorescence, $\Delta F(t)/F$, that exceeded a threshold value, generally a 10% increase. To obtain a conservative determination of the rate of fluorescence transients, we imposed a minimum interval, generally 10 s, between the individual fluorescence peaks detected within each ROI to prevent redundant detection of multiple peaks within individual events (Figure 3B). To avoid including noisy signals resulting in high false positive detection rates, we excluded ROIs that showed >5 times the median rate of Ca^{2+}-transients for each movie.

Calculation of Event Rates and Confidence Intervals.

Confidence intervals for all event rates that we report were estimated by making the statistical assumption that the number of event occurrences is Poisson distributed.

Statistical Tests of Significant Difference

We used two-tailed Wilcoxon rank sum tests to assess the significance of differences between median Ca^{2+} transient characteristics in each of the five experimental conditions: anesthetized, awake, TTX-, γDGG-, and PPADS-treated awake. For analyzing the anisotropic spread of Ca^{2+} during bursts (see below), we hypothesized that the spread in the direction parallel to the cerebellar folium is greater than the spread perpendicular to the folium. To test this, we used a Wilcoxon signed rank test of the hypothesis that the difference between the two radii has a median of zero. Because we measured a large number of individual events (n = 95 across all conditions), we used a normal approximation for the distribution of the test statistic to compute the *p*-value.

To test the significance of differences in the frequencies of sparkles and bursts across the different pharmacological conditions used within individual experiments, we used a likelihood ratio test based on the assumption that the numbers of events were Poisson distributed. In each condition, i, we observed n_i events in time t_i over a field of view area a_i. The maximum likelihood estimate of the event rate was thus $r_i = n_i/(t_i a_i)$. To test whether the rates under the two different conditions were significantly different, we used a likelihood ratio test. This compared the likelihoods of obtaining the total $n_i + n_j$ events given two distinct rates for the two experiments versus with one estimated rate, $(n_i + n_j)/(t_i a_i + t_j a_j)$, for both conditions. The resulting likelihood ratio:

$$LR = \frac{r_i^{n_i} r_j^{n_j}}{\left[(n_i + n_j)/(t_i a_i + t_j a_j)\right]^{(n_i + n_j)}}.$$

has an associated *p*-value, which is found by calculating $\chi^2 = -2\log(LR)$ and comparing with the cumulative chi-square distribution with 1 degree of freedom.

Analysis of Ca^{2+} Sparkles

Sparkles were detected within individual glial ROIs as described above. The duration of each event was defined as the interval from when the signal first exceeded the detection threshold (10% $\Delta F(t)/F$) to when the signal returned below this level.

Analysis of Ca^{2+} Bursts

Analysis of Two-Dimensional Spatial Profiles

We identified the approximate location and onset time of each burst by visual inspection of the normalized fluorescence data. Only events that did not extend beyond the recording field of view were used for further analysis of spatial profiles. For each event we computed the maximum of the normalized fluorescence in each pixel during the first 7 s after event onset. We rotated the resulting image to align it with a local coordinate system in which the long axes of Purkinje cell dendrites were oriented along the *y*-axis. We then

used nonlinear least squares regression (Levenberg-Marquardt algorithm; MATLAB routine *nlinfit*) to fit the shape of the maximum intensity profile with a two-dimensional Gaussian function. The fit was constrained to have its principal axes oriented along the *x* and *y* directions. This fitting procedure produced reasonable estimates of burst spatial extent, as judged by inspection of the fit and its residual, even in cases in which animal movement or blood flow influenced the maximum intensity projection. However, for the bursts of greatest magnitude we noticed that the maximum intensity projection deviated from the fitted Gaussian, exhibiting a flatter central region and more sharply defined edges. The diameters parallel and perpendicular to the folium plotted in Figure 4F were defined as four times the standard deviation values from the Gaussian fit.

Analysis of Three-Dimensional Spatial Profiles

To characterize the volumetric structure of bursts, we analyzed as described above each of the lateral planes sampled within the three-dimensional (3D) recording. We smoothed individual image frames by convolution with a Gaussian that had a standard deviation of 1 pixel, approximately 2 μm across. Because the pixel spacing in the axial dimension was about 5 μm, or roughly twice as large as the lateral pixel spacing, we linearly interpolated the data at planes midway between each scan plane. We also smoothed the temporal dynamics, as described above.

The normalized fluorescence data, represented as a four-dimensional array of intensity values at every spatial point (*x, y, z*) and time frame (*t*), were examined in three ways. We inspected the complete set of information available about each event from the collection of movie frames acquired across a series of optical planes (Figure 4A, Movie S1). We viewed the maximal spatial extent of each event using projections of maximum intensity over time and one spatial dimension into the *x*-*y*, *x*-*z*, and *y*-*z* planes. Finally, to compare multiple events recorded within the same imaging volume, we used a sequence of contours, each of which represented the spatial extent of the burst at a distinct depth beneath the brain surface (Figure 4E).

We determined the contours using the maximum intensity projection over time for each event. We smoothed each *z*-slice of these projections by convolving with a Gaussian (5 μm s.d.), and applied a threshold to the result to produce a binary mask of the region for which $(\Delta F(t)/F)_{max} \geq 15\%$. Isolated pixels or groups of pixels that were not contiguous with the main volume of the event were excluded. We used the remaining connected volume to create the contours at each imaging plane (Figure 4E).

The grayscale background images in Figure 4E show the patterns of OGB-1-AM labeling at the boundaries of the imaging volume. The areas covered by the contours of each burst, as projected onto the *x*-*y* plane, are shown at the bottom of Figure 4E. The cross-sectional area at each scan plane was used to assess the depth profile of the events.

To quantify the spatial extent and total volume of bursts in 3 spatial dimensions, we computed the maximum normalized fluorescence intensity at each pixel during the first 7 s of each event recorded during 3D imaging experiments. We excluded events that occurred near any of the lateral edges of the imaging volume. Because the frame rate for volumetric imaging (~1-2.5 Hz) was lower than the frame rate for 2D-imaging, we chose to smooth the event shape in each imaging plane using a Gaussian spatial filter (5 μm s.d.), rather than using a temporal filter as in 2D analysis. The filter width was chosen to match the minimum spacing between imaging planes in the axial dimension. We fit the event shape with a three-dimensional Gaussian ellipsoid with eight free parameters (3 coordinates for the center of mass, 3 independent spatial widths, background intensity, and event amplitude). To correct for the systematic bias introduced into the fit parameters by Gaussian convolution, we subtracted the variance of the smoothing filter from the fit variances. The volume of each event was defined as the volume of the ellipsoid contained within two standard deviations:

$$V = \frac{4}{3}\pi(2\sigma_x)(2\sigma_y)(2\sigma_z).$$

Analysis of Temporal Dynamics

To characterize the temporal dynamics of bursts, we used the average fluorescence over the 7 s preceding the event onset to estimate background fluorescence. We then averaged fluorescence changes across an elliptically shaped ROI defined as the boundary at which the Gaussian spatial fit to the event (see above) falls to 1/*e* of its peak value. We found that the normalized fluorescence traces were well fit (r = 0.9 ± 0.1 s.d.) by a convolution of two exponentials, which has four free parameters, amplitude (A), onset time (t_0), and two rate constants (k_1 and k_2):

$$f(t) = \begin{cases} 0 & t < t_0 \\ A \dfrac{e^{-k_2(t-t_0)} - e^{-k_1(t-t_0)}}{(k_2/k_1)^{k_2/(k_1-k_2)} - (k_2/k_1)^{k_1/(k_1-k_2)}} & t \geq t_0 \end{cases}.$$

We employed MATLAB's Trust-Region nonlinear least squares solver with constraints to perform the fits, which were then used to align and normalize the individual traces and to compute the average of the normalized traces in each experimental condition (Figure 4B). In many cases (81% of bursts observed in the control condition), the best fit time constants were equal, $k_1 = k_2$, to within 1%. In this case the fit has the same form as a first-order alpha function with a single rate constant:

$$f(t) = \begin{cases} 0 & t < t_0 \\ Ak(t-t_0)e^{1-k(t-t_0)} & t \geq t_0 \end{cases}.$$

Analysis of Ca^{2+} Flares

Analysis of Locomotor Speed

We smoothed and downsampled to ~20 Hz the data from the optical encoder that reports the rotational velocity of the exercise ball. We further smoothed the signal in time (Gaussian filter, s.d. of 0.7 s). The onset of locomotion was defined as the time at which the smoothed running speed increased over a threshold of 20 mm/s. Offset was defined as the time at which the speed subsequently fell below 10 mm/s. These thresholds were chosen to avoid the detection of small movements and to ignore small dips in speed during otherwise continuous bouts of running.

Detection of Ca^{2+} Flares

Within each palisade fiber ROI we first detected all events in which a local peak in the smoothed fluorescence signal was achieved and exceeded a fixed threshold (see above; threshold was 10% $\Delta F(t)/F$ and minimum inter-event interval was 10 s). We calculated the mean instantaneous rate of glial Ca^{2+} events within the field of view by counting all events occurring at each movie time frame, and multiplying by the frame rate and dividing by the field of view area. The rate of glial Ca^{2+} events was then smoothed using a Gaussian filter (see above; Gaussian s.d. was 2 s). The onset and offset times of Ca^{2+} flares were defined analogously to the detection of movements by the times at which the smoothed rate crossed a threshold. Because of differences in the signal/noise ratio across experiments, we adjusted these thresholds manually for each recording within the range from 10-220 Hz/mm^2. For this analysis we excluded epochs of ~10 s duration around the time of each burst, resulting in minimal loss of data since bursts occurred very sparsely.

Movement-Triggered Averaging of Glial Ca^{2+} Signals

We examined how Ca^{2+} flares depend on two aspects of locomotor behavior. We first studied the impact of the duration of running bouts on the physiological event dynamics. We assigned movements to three categories containing either all movements, brief movements (<5 s duration from onset to offset), or extended movements (>15 s duration). To prevent interference from recently completed bouts of running (see below), we excluded movements that began within a short time (10 s) after the offset of another movement or, for the first movement in each recording, after the start of the recording. For every movement in each of the three duration categories, we determined whether the corresponding signal (Ca^{2+} event rate in Bergmann glial fibers) during a period from 10 s before to 25 s after movement onset exceeded a threshold (20 Hz/mm^2). We aligned all such signals to the start of the movement and computed the average (Figure 6C).

Next we examined the impact of the pause duration, defined as the time from the offset of the previous bout of movement to the onset of the current movement, on the probability of observing a Ca^{2+} flare (Figure 6D). We classified all movements based on their inter-movement pause into logarithmically spaced bins. For this analysis we excluded the first running bout in each recording, for which we could not determine the pause time. For each movement we determined whether there was a supra-threshold increase in the corresponding glial Ca^{2+} event rate signal within 10 s of movement onset. Within each bin, the probability of a physiological response at movement onset was defined as the number of movements accompanied by a supra-threshold increase in the physiological signal divided by the total number of movements. We estimated 68% confidence intervals for our determinations of response probability by assuming the responses were governed by a binomial distribution. We performed a logistic regression to fit the binary flare occurrence data to a two-parameter sigmoid:

$$P = \frac{1}{1 + (IMI/IMI_0)^x},$$

where IMI is the inter-movement interval and IMI_0 is a fit parameter corresponding to the pause value for which the probability of flare occurrence was 50%. The fit parameters for the line shown in Fig. 4D were IMI_0 = 27.5 s and x = -1.42.

Analysis of Somatic Bergmann Glial Ca^{2+} Transients

Ca^{2+}-transient related increases in fluorescence within individual somatic ROIs were identified by finding peaks in the smoothed normalized fluorescence, $\Delta F(t)/F$, that exceeded a threshold value, generally a 10% increase.

General Methods of Laser Doppler Flowmetry

We tracked blood perfusion levels using a laser Doppler instrument (PF-5010-LDPM, Perimed) with a 1-mm diameter fiber-optic probe (PR 407-1) that we affixed either to the cranium or an optical window using a miniature probe holder (PH 07-6). A smoothing filter with a 0.03 s time-constant was applied to all perfusion traces. Perfusion measurements were performed either through the intact skull or using the same preparation as described in Experimental Procedures, Animals and Surgery and in Supplemental Experimental Procedures, Pharmacology. To assess the extent of motion artifacts, we performed control experiments by placing the fiber-optic probe in a colloidal suspension of latex particles (PF 1001, Perimed) that is normally used for probe calibration, within either the miniature probe holder or the head of the screw connecting the head plate and head holder.

Analysis of Laser Doppler Flowmetry Signals

We normalized laser Doppler signals by dividing by the median signal during non-movement periods, defined as when the speed of the exercise ball was <10 mm/s. We then detected transient increases in blood perfusion (Figure 7) in a manner analogous to the detection of exercise ball rotation and Ca^{2+} flares (see above; the thresholds for blood perfusion event onset and offset were 15% and 10%, respectively).

Pressure Application

To test whether Ca^{2+} flares can be evoked by tissue displacements that might occur during locomotor activity, we exerted mechanical stimuli to the head holder or cranial window, both in mice under isoflurane anesthesia and in awake mice, during Ca^{2+}-imaging sessions. Pressure stimuli of various amplitudes, frequencies and durations were applied using a glass rod (1.0 mm outer diameter; A-M Systems, Inc.) mounted to a micromanipulator (Sutter Instrument Company) that was controlled manually. In some cases, bidirectional pressure stimuli were delivered manually to the head holder or cranial window using angled forceps (Fine Science Tools).

Electrical Stimulation of Limbs

To test whether Ca^{2+} flares can be evoked by peripheral stimulation, we electrically stimulated the limbs while the mouse was under anesthesia. Electrical stimuli were delivered via a pair of 30-gauge needles attached to a stimulus isolator (Isostim A320; World Precision Instruments) and connected to a 12-bit high-speed 1MS/s analog output board (PCI-6711, National Instruments). Stimulation was controlled by custom software written in LabVIEW (Version 7.1; National Instruments) and consisted of a train of 60 square pulses, each of 20 ms duration and 0.5-10 mA amplitude, delivered at 20 Hz. Electrical stimulation caused limb withdrawal that was highly noticeable. Signals delivered to the stimulation needles were recorded at 10 kHz simultaneously with optical recordings, using MP-Scope data-acquisition software (see above).

SUPPLEMENTAL REFERENCES

Nguyen, Q.T., Tsai, P.S., and Kleinfeld, D. (2006). MPScope: A versatile software suite for multiphoton microscopy. Journal of Neuroscience Methods *156*, 351-359.

Nimmerjahn, A., Kirchhoff, F., Kerr, J.N.D., and Helmchen, F. (2004). Sulforhodamine 101 as a specific marker of astroglia in the neocortex in vivo. Nat Methods *1*, 31-37.

Piet, R., and Jahr, C.E. (2007). Glutamatergic and purinergic receptor-mediated calcium transients in Bergmann glial cells. J Neurosci *27*, 4027-4035.

Stosiek, C., Garaschuk, O., Holthoff, K., and Konnerth, A. (2003). In vivo two-photon calcium imaging of neuronal networks. Proc. Natl. Acad. Sci. U. S. A. *100*, 7319-7324.

Thevenaz, P., Ruttimann, U.E., and Unser, M. (1998). A pyramid approach to subpixel registration based on intensity. IEEE Transactions on Image Processing *7*, 27-41.

Tomomura, M., Rice, D.S., Morgan, J.I., and Yuzaki, M. (2001). Purification of Purkinje cells by fluorescence-activated cell sorting from transgenic mice that express green fluorescent protein. European Journal of Neuroscience *14*, 57-63.

Zuo, Y., Lubischer, J.L., Kang, H., Tian, L., Mikesh, M., Marks, A., Scofield, V.L., Maika, S., Newman, C., Krieg, P., and Thompson, W.J. (2004). Fluorescent proteins expressed in mouse transgenic lines mark subsets of glia, neurons, macrophages, and dendritic cells for vital examination. J Neurosci *24*, 10999-11009.